IEEE Robotics and Automation Letters (RAL) paper presented at
2024 IEEE/RSJ International Conference on Intelligent Robots and Systems (IROS)
October 14-18, 2024. Abu Dhabi, UAE

Experimental Validation of a 7-DOF Power Soft Robot Driven by Hydraulic Artificial Muscles

Yunhao Feng, Tohru Ide, Hiroyuki Nabae, *Member, IEEE*, Gen Endo, *Member, IEEE*, Ryo Sakurai, Shingo Ohno, and Koichi Suzumori, *Senior Member, IEEE*

***Abstract*—Hydraulic artificial muscles offer superior performance compared to most pneumatic artificial muscles, but their suitability in multi-DOF robotics remains unverified. We fabricated a 7-DOF power soft robot spanning over 1.5 m using 29 McKibben hydraulic artificial muscles. We analyzed the proposed robot's workspace, payload capacity, and compliance based on the properties of the hydraulic muscles and conducted several validation experiments. The robot successfully handled a payload of more than 25 kg at a maximum pressure of 5.0 MPa and exhibited passive compliance ranging from 0.5 to 2.0 mm/N with valves fully closed. Furthermore, the robot demonstrated strong impact resistance and successfully performed tasks such as concrete chipping. These results demonstrate the capability of muscle-driven robots to perform diverse tasks in a range of industrial environments.**

***Index Terms*—Hydraulic/pneumatic actuators, mechanism design, soft robot materials and design.**

I. Introduction

CONVENTIONAL industrial robots use heavy and rigid actuators for heavy tasks but often lack crucial safety features for human-robot interactions. In contrast, robots with compliant soft actuators [1], [2], [3], [4], [5], [6] lack strength and stability for tasks requiring high forces accompanied by strong disturbances. Suzumori et al. introduced the "Power Soft Robot" concept, which combines powerfulness and softness [7]. A suitable actuator is the hydraulic artificial muscle (HAM), known for its key characteristics:

- Powerful yet lightweight: HAMs offer a strength-to-weight ratio of 5 to 10 times higher than conventional electric motors or hydraulic cylinders.
- Durable yet tough: Highly durable, oil-resistant rubber enables these HAMs to effectively withstand strong impacts and vibrations.
- Gentle yet controllable: HAMs are suitable for tasks requiring strong force and delicate force control.

Manuscript received 10 November 2023; accepted 1 April 2024. Date of publication 26 April 2024; date of current version 2 May 2024. This letter was recommended for publication by Associate Editor S. Song and Editor Y.-L. Park upon evaluation of the reviewers' comments. This work was supported in part by the JSPS KAKENHI Grant-in-Aid for Scientific Research(A) under Grant JP18H03760 and in part by Toshiba Corporation. *(Corresponding author: Yunhao Feng.)*

Yunhao Feng, Tohru Ide, Hiroyuki Nabae, Gen Endo, and Koichi Suzumori are with the Department of Mechanical Engineering, Tokyo Institute of Technology, Meguro-ku 152-8550, Japan (e-mail: feng.y.ac@m.titech.ac.jp).

Ryo Sakurai and Shingo Ohno are with Bridgestone Corporation, Kodaira-shi 187-8531, Japan.

This letter has supplementary downloadable material available at https://doi.org/10.1109/LRA.2024.3394219, provided by the authors.

Digital Object Identifier 10.1109/LRA.2024.3394219

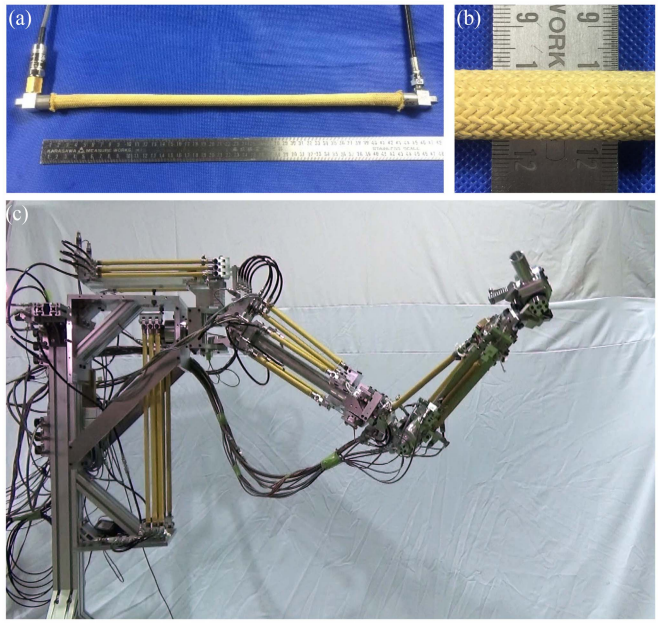

Fig. 1. 7-DOF power soft robot driven by hydraulic artificial muscles (HAMs): (a) Depiction of a hydraulic artificial muscle. (b) Outer sleeve of the muscle knitted at a 30° angle for enhanced durability in high-pressure environments. (c) Overall appearance of the 7-DOF power soft robot.

While prior studies have focused on developing multi-DOF robots using pneumatic artificial muscles (PAM) [8], [9], [10], [11], [12], [13], as well as devices utilizing HAMs [14], [15], [16], [17], there is limited research on the multi-DOF robots employing HAMs. Pressure is crucial for fluid-driven robots, from large to micro ones [18]. HAMs handle up to 5.0 MPa, while PAMs typically operate below 0.7 MPa. Multi-DOF HAM robots offer superior force, stiffness, and stability, potentially enabling operations considered challenging for PAM robots, though experimental validation is still lacking. On the other hand, many current robots struggle with tasks like hammering or operating in collision-prone environments because they lack impact and vibration resistance due to rigid components prone to damage and insufficient damping mechanisms. A robust power soft robot using HAMs offers effective impact and vibration absorption, potentially enhancing reliability in various applications. However, this also requires experimental validation.

In this study, we developed a 7-DOF power soft robot utilizing twenty-nine HAMs, reaching pressures of 5.0 MPa. We verified the practicality of the power soft robots through experiments analyzing performance like workspace and payload

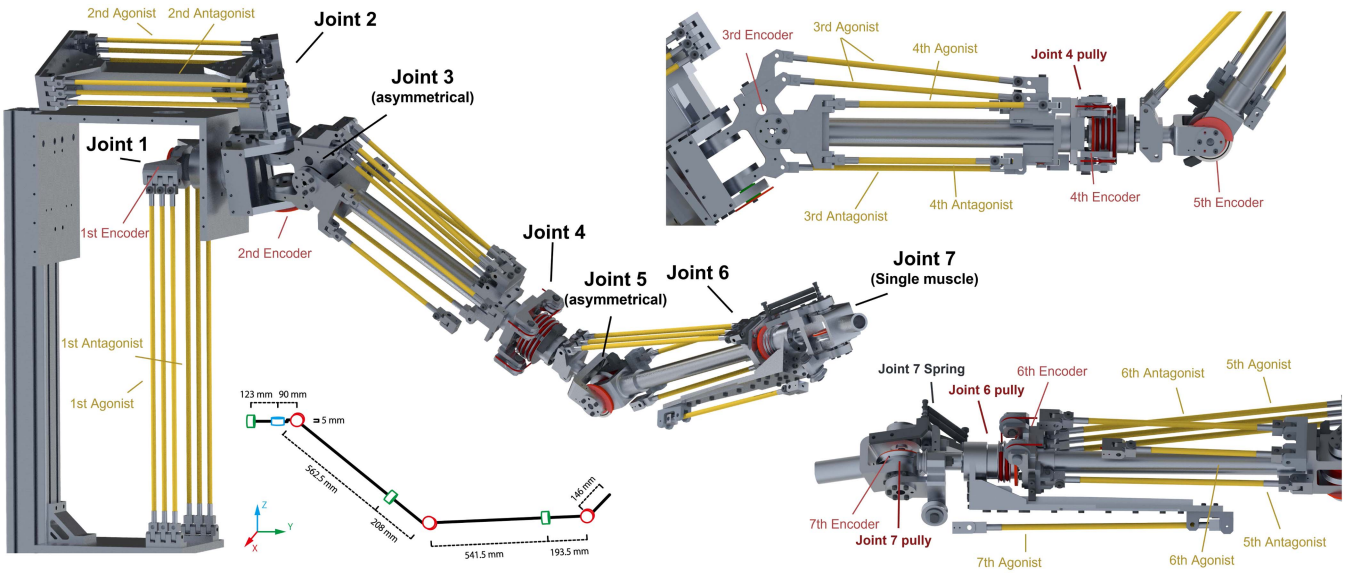

Fig. 2. Mechanical design of the 7-DOF power soft robot: Joint design and muscle/encoder positions, excluding hydraulic components (hoses and pressure transmitters). The 3rd and 5th antagonistic joints have asymmetrical designs, while the 4th and 6th antagonistic joints utilize cable-pulley mechanisms.

TABLE I
MUSCLE CONFIGURATION IN MECHANICAL DESIGN

Joint no.		Shoulder				Elbow		Wrist	
		1	2	3		4	5	6	7
Agonist side	Muscle length	729 mm	400 mm	337 mm (Lower)	406 mm (Upper)	303 mm	472 mm	297 mm	268 mm
	Contraction ratio	16.2%	23.0%	17.0%	22.7%	24.8%	25.6%	16.2%	16.9%
	Muscle number	3	3	3	2	2	3	1	1
Antagonist side	Muscle length	729 mm	400 mm	348 mm		303 mm	333 mm	297 mm	-
	Contraction ratio	16.2%	23.0%	12.1%		24.8%	12.3%	16.2%	-
	Muscle number	3	3	1		2	1	1	-
Designed movable range		66°	50°	40°		90°	60°	90°	65°
Features		Sym.	Sym.	Asym.		Sym. Pully-driven	Asym.	Sym. Pully-driven	Non-Antagonistic

capacity, characterization of compliance and impact resistance, and conducting actual construction site operations. We introduce the robot design and theoretical analysis of its characteristics in Section II, followed by multiple validation experiments in Section III. Finally, Section IV presents the conclusions.

II. 7-DOF POWER SOFT ROBOT

A. Mechanical Design and Control System

The power soft robot is shown in Fig. 1, which is more than twice the average length of a human arm. The muscles in the robot are designed to contract in the axial direction without bending. The mechanical design of all joints is shown in Fig. 2, and the HAM configurations are detailed in Table I, where the muscle length refers to the contractible length of a muscle. The joints are mostly antagonistic, controlled by agonist-antagonist muscle pairs. Cable-pulley mechanisms are employed in the 4th and 6th antagonistic joints. The 3rd and 5th joints are asymmetrical antagonistic joints designed with more muscle on the upper side than on the lower side to enhance lifting capability. The robot employs artificial muscles ranging from 268 to 729 mm in length, with dry weights ranging from 100 to 160 g. The muscle specifications are given in Table II. The weight of the arm section is at approximately 40 kg class using CAD mass estimation.

We utilize seven servovalves to control all joints, ensuring a low-cost solution [19]. Fourteen hydraulic pressure transmitters were utilized to monitor muscle pressure and supply pressure, complemented by seven optical incremental encoders for angular positions. The servovalves, transmitters, and encoders were interfaced with a dSPACE MicroLabBox controller and controlled within the MATLAB/Simulink environment. During the experiments, the supply pressure was capped at approximately 5.6 MPa, while the internal pressure of the muscles ranged from 0.5 to 5.0 MPa.

TABLE II
SPECIFICATIONS OF THE HAM

Outer sleeve braid angle	30°
Rubber tube outer diameter	12.0 mm
Rubber tube inner diameter	6.6 mm
Rubber tube thickness	2.7 mm
Outer diameter (natural length)	14.5 mm
Pressurized outer diameter (natural length)	Max. 16.0 mm

Unit length muscle mass (contractible part)	1.14 g/cm
Terminal mass	37 g
Unit length internal volume	0.342 cm^3/cm
Operating pressure range	0 to 5.0 MPa
Maximum contraction force	2.8 kN
Maximum contraction ratio	26%

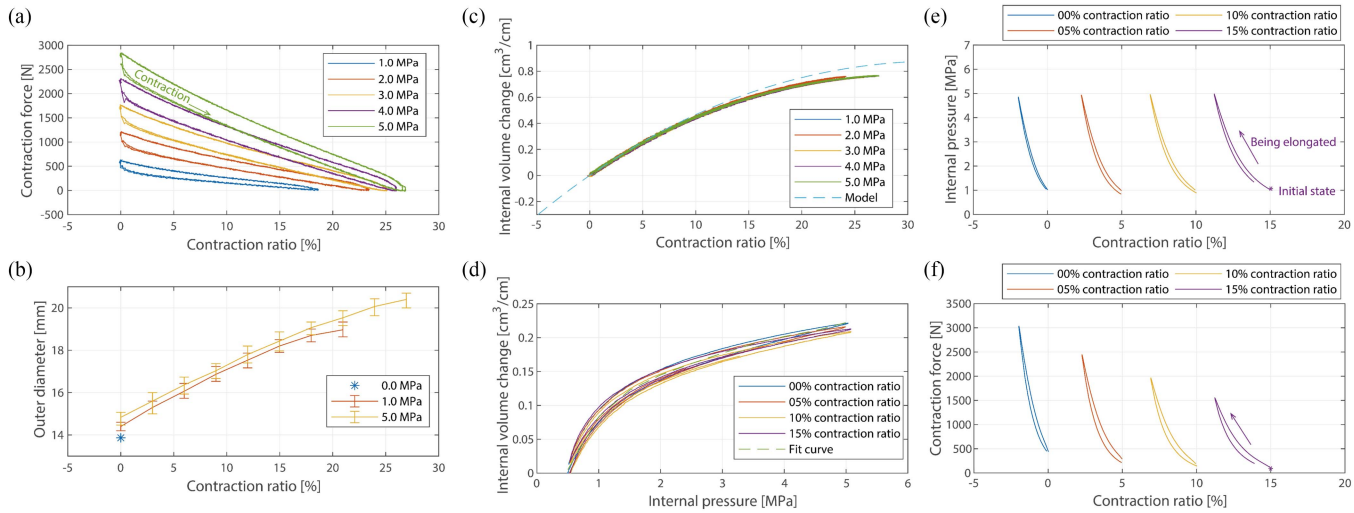

Fig. 3. Characteristics of the HAMs used in the power soft robot: (a) Relationship between contraction force and contraction ratio at different pressures. (b) Relationship between outer diameter and contraction ratio at different pressures. (c) Relationship between contraction ratio and internal volume change per unit length. (d) Relationship between pressure and internal volume change at different contraction ratios per unit length. (e) Pressure changes due to elongation by external force when the valve is closed (internal volume remains unchanged, and contraction ratio is forced to decrease). (f) Change in contraction force due to elongation by external force when the valve is closed.

In this study, our primary focus was to validate the performance of the robot hardware. As such, we utilized the widely adopted pseudoinverse-based inverse kinematics method to regulate both the end-effector position and orientation. The Jacobian matrix combines homogeneous transforms for position and quaternions for orientation to prevent singularities. The deviation of joint positions from the median of the motion range is minimized to prevent excessive muscle contraction by utilizing redundancy. Positional PI controllers with dynamic integrator clamping were employed to control servovalves, alongside the implementation of saturation limits to restrict speed and prevent joint runaway.

B. Static Model of HAM Joint

1) Hydraulic Artificial Muscle: Here, a 334 mm muscle serves as a reference, with its contraction force and outer diameter change depicted in Fig. 3(a) and (b). The muscle exhibits a maximum contraction force and ratio of approximately 2800 N and 26%, respectively. We simplify the contraction force F with pressure P as follows:

$$F = (K_{\mathrm{f}} P - \mathrm{sgn}(\dot{\epsilon}) K_{\mathrm{hys}})(\epsilon_{\max} - \epsilon) \tag{1}$$

where $\mathrm{sgn}(\dot{\epsilon})$ accounts for hysteresis effects, K_{f} and K_{hys} are the coefficients obtained in Fig. 3(a), respectively, ϵ is the contraction ratio, $\epsilon_{\max}$ is the maximum contraction ratio.

After pressurization, the outer diameter slightly increases, gradually expanding further with increasing contraction ratio. The radial expansion allows the muscle to be elongated while maintaining the internal volume. The changes in volume during contraction and pressurization are shown in Fig. 3(c) and (d). Furthermore, Fig. 3(e) and (f) illustrates the changes in pressure and contraction force when the muscle is elongated, demonstrating its passive compliance. The volume change ΔV_ϵ due to contraction ratio change ($\epsilon_{\mathrm{ori}} \to \epsilon_{\mathrm{new}}$), and the volume change ΔV_{P} due to pressure change ($P_{\mathrm{ori}} \to P_{\mathrm{new}}$) can be approached as follows:

$$\begin{aligned} \Delta V_\epsilon(\epsilon_{\mathrm{ori}}, \epsilon_{\mathrm{new}}) &= V_\epsilon(\epsilon_{\mathrm{new}}) - V_\epsilon(\epsilon_{\mathrm{ori}}) \\ V_\epsilon(\epsilon) &= \frac{b^2 - {L_\epsilon}^2}{4n^2}\pi L_\epsilon - \frac{d_{\mathrm{rub}}^2 - d_{\mathrm{in}}^2}{4}\pi L \end{aligned} \tag{2}$$

$$\begin{aligned} \Delta V_{\mathrm{P}}(P_{\mathrm{ori}}, P_{\mathrm{new}}) &= V_{\mathrm{P}}(P_{\mathrm{new}}) - V_{\mathrm{P}}(P_{\mathrm{ori}}) \\ V_{\mathrm{P}}(P) &= (a_1 P^5 + \cdots + a_5 P + a_6) L \end{aligned} \tag{3}$$

b is the fiber length, n is the turn of fiber, L is the muscle length and L_ϵ is the contracted length with contraction ratio ϵ, d_{rub} and d_{in} are the rubber inner and outer diameters, respectively. $V_{\mathrm{P}}(P)$ using polynomial approximation with coefficients $\{a_1, \ldots, a_6\}$, the fit curve is shown in Fig. 3(d).

The contraction force generated F_{dis} due to a small muscle contraction displacement ΔL can be given by the following equation. When the valve is fully closed (constant internal volume), ΔP satisfies that the volume error $\delta V_{ij} = |\Delta V_{\mathrm{P}}(P, P + \Delta P) - \Delta V_\epsilon(\epsilon, \epsilon - \Delta L/L)|$ approaches 0, indicating that the volume change caused by pressure and contraction change is the same. Compared to PAMs, HAMs using non-compressible fluids have a very large ΔP for small contraction changes, making

Algorithm 1: Payload of the Power Soft Robot.

Input: A initial *pose* with $\theta_1, \ldots, \theta_7$
Output: Payload capacity of reachable *pose*
Compute each Jacobian J_{gi} to i-th link centre-of-mass
Joint torques for arm weight: $\boldsymbol{\tau}_g \leftarrow \sum_{i=1}^{7}(J_{gi}^{T}F_{gi})$
for joint $i = 1$ to 7 **do**
  Compute ϵ_{ij}, A_{ij} for each muscle on i-th joint
  Compute joint torque range $[\tau_i(\theta_i, 5, 0), \tau_i(\theta_i, 0, 5)]$
end for
if $\tau_{gi} \in [\tau_i(\theta_i, 5, 0), \tau_i(\theta_i, 0, 5)]$ for all joints **then**
  Mark *pose* as a reachable pose
  repeat
    Update joint pressure difference ΔP_i
    $[P_{ti}, P_{ai}] \leftarrow [P_{avg} - \Delta P_i, P_{avg} + \Delta P_i]$
  until $|\tau_i(\theta_i, P_{ti}, P_{ai}) - \tau_{gi}| < torquetolerance$
  Compute margin of $\tau_i(\theta_i, \ldots)$ within torque range
  Compute payload capacity using torque margin
else
  Mark *pose* as a unreachable pose
end if

Algorithm 2: Compliance of the Power Soft Robot.

Input: A reachable *pose* with $\theta_1, \ldots, \theta_7, P_{t1}, \ldots, P_{ti}, P_{ai}$
Output: Compliance of the reachable *pose*
Compute Jacobian J to end-effector with $\theta_1, \ldots, \theta_7$
Joint torques for force F: $\boldsymbol{\tau}_f \leftarrow J^{T}F$
switch *compliancetype* **do**
  case *pressureconstant* :
    repeat
      Update all joint displacements $d\boldsymbol{\theta}$
      Compute ϵ_{ij}, A_{ij} for every muscle
      i-th joint torque: $\tau_i \leftarrow \tau_i(\theta_i + d\theta_i, P_{ti}, P_{ai})$
    until $\max(|\boldsymbol{\tau} - (\boldsymbol{\tau_g} + \boldsymbol{\tau_f})|) < torquetol$
  Case *volumeconstant* :
    repeat
      Update all joint displacements $d\boldsymbol{\theta}$
      Compute ϵ_{ij}, A_{ij} for every muscle
      repeat
        Update P_{ti}, P_{ai} for i-th joint
        Volume error: $\delta V_{ij} \leftarrow |\Delta V_{Pij} - \Delta V_{\epsilon ij}|$
      until $\max([\delta V_{11}, \ldots, \delta V_{ij}]) < pressuretol$
      i-th joint torque: $\tau_i \leftarrow \tau_i(\theta_i + d\theta_i, P_{ti}, P_{ai})$
    until $\max(|\boldsymbol{\tau} - (\boldsymbol{\tau_g} + \boldsymbol{\tau_f})|) < torquetol$
Compute *newpose* with $\boldsymbol{\theta} + d\boldsymbol{\theta}$ as displaced pose
Compute displacement between *newpose* and *pose*

them less compliant than PAMs.

$$F_{dis} = \left(\frac{K_f P}{L}\right)\Delta L + K_f(\epsilon_{max} - \epsilon)\Delta P \tag{4}$$

2) Antagonistic Joint: Assuming a joint with m muscles, each muscle has an angle $A_j(\theta)$ with the lever ($A_j(\theta) > 0$ for the agonist side, $A_j(\theta) < 0$ for the antagonist side) or a pully ($A_j(\theta)$ is constant 90° or −90°), and a distance r_j to the rotational center. Muscle pressure can be agonistic-side pressure P_a or antagonistic-side pressure P_t, The torque produced is the sum of the torques generated by all the muscles, given as follows,

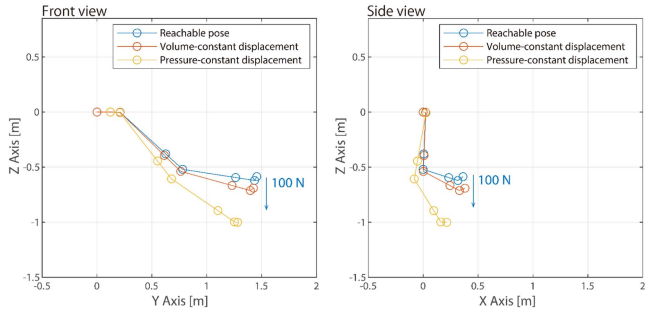

Fig. 4. Example of reachable pose and corresponding compliance in simulation: a reachable pose obtained from Algorithm 1 and its volume-constant and pressure-constant compliance under 100 N force obtained from Algorithm 2.

ignoring hysteresis:

$$\tau(\theta, P_t, P_a) = \sum_{j=1}^{m} \sin A_j K_f P_j(\epsilon_{max} - \epsilon_j) r_j$$
$$P_j \in \{P_t, P_a\} \tag{5}$$

The torque τ_{dis} caused by very small displacement $\Delta\theta$ and muscle pressure change ΔP_j can be calculated as follows:

$$\tau_{dis} = \sum_{j=1}^{m} K_f \left(\sin A_j(\epsilon_{max} - \epsilon_j) r_j \Delta P_j - \sin|A_j| \frac{P_j r_j^2}{L_j}\Delta\theta\right) \tag{6}$$

For (6), it applies only to small joint displacements. Thus, we introduce an iterative simulation for a more accurate analysis of the power soft robot.

C. Simulation Analysis of Power Soft Robot

1) Workspace and Payload: We employ the Monte Carlo method within the MATLAB environment to determine the reachable workspace by randomly sampling poses, following Algorithm 1. The average pressure P_{avg} is set as 2.5 MPa. A pose is considered reachable if the torques required for the arm weight fall within allowable torque limits for all joints. At a maximum muscle pressure of 5.0 MPa, the torque range of the i-th joint at an angle θ_i is $[\tau_i(\theta_i, 5, 0), \tau(\theta_i, 0, 5)]$. The payload capacity is considered as the maximum Z-directional force exerted by the end-effector, ensuring that the combined torque resulting from the arm weight τ_{gi} and the torque required to generate force τ_{fi} falls within the range of $\tau_{gi} + \tau_{fi} \in [\tau_i(\theta_i, 5, 0), \tau(\theta_i, 0, 5)]$ for each joint. An example of reachable poses is illustrated in Fig. 4. For reachable poses, we compute the payload capacity. The volume envelope encompassing all reachable poses is depicted in Fig. 5(a) as reachable workspace. Fig. 5(b) shows the relationship between payload and end-effector positions.

The robot exhibits a notable payload capacity, lifting up to 25 kg within a range of less than 1.0 m below the shoulder. With the end-effector in a lower position, the shoulder joints produce more lifting torque, thereby providing higher lifting force. Above shoulder height, the payload capacity is lower mainly due to the muscles behind in 1st joint exert less force with higher contraction ratios. The experimental results for workspace and payload capacity are depicted in Fig. 6.

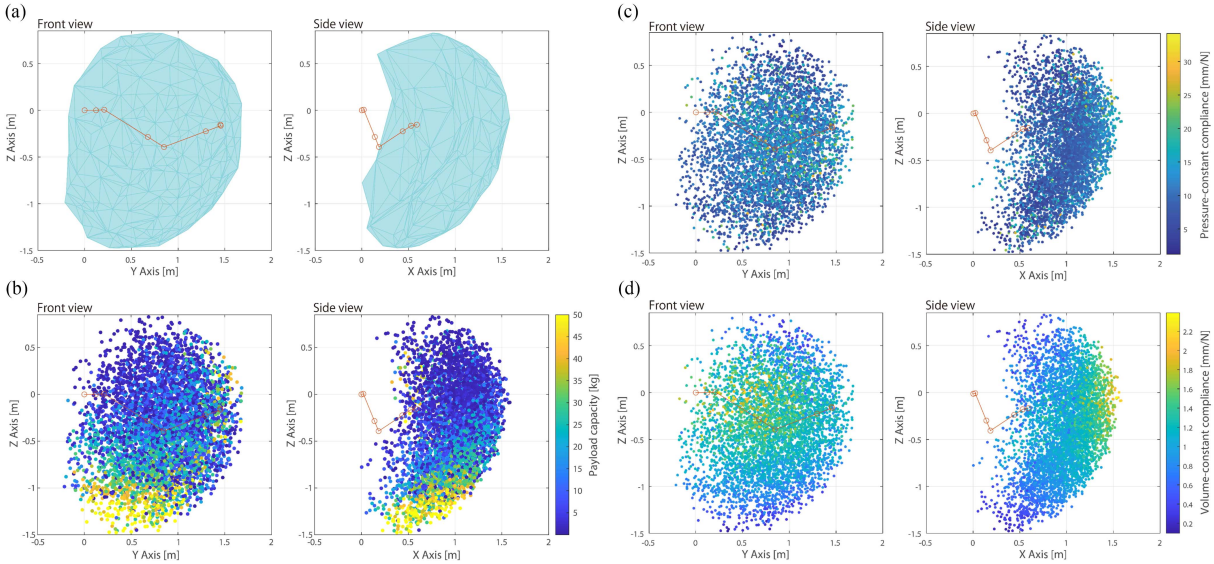

Fig. 5. Reachable workspace, payload capacity, and compliances of the power soft robot: (a) Reachable workspace of the power soft robot. (b) Payload capacity of all reachable poses used for volume envelopes of the workspace. (c) End-effector vertical pressure-constant compliance with 1 N downward force. (d) End-effector vertical volume-constant compliance with 1 N downward force.

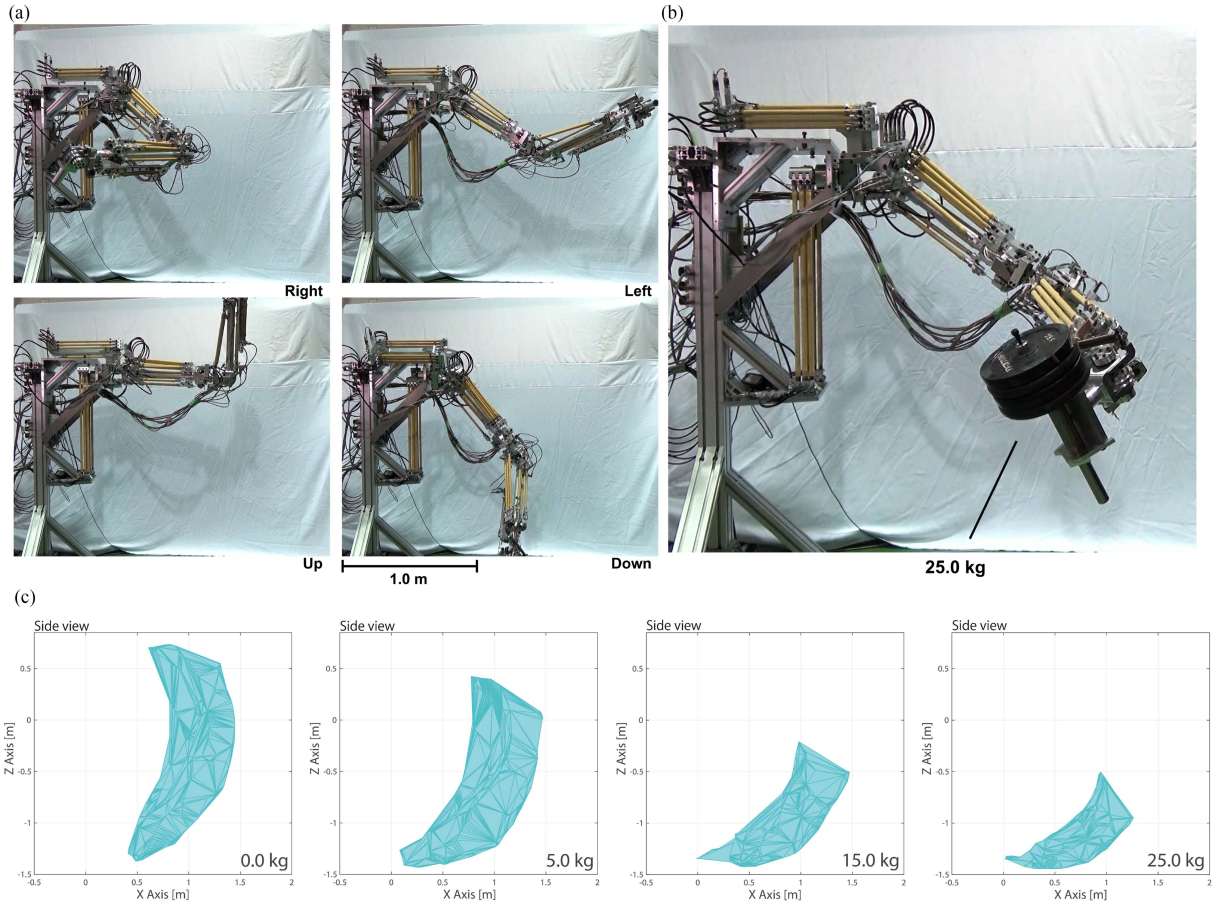

Fig. 6. Experimental workspace and payload capacity of the 7-DOF power soft robot: (a) Reachable poses in four directions. (b) The power soft robot lifting a 25-kg load. (c) Relationship between payload and reachable workspace: with a higher payload, the workspace of the power soft robot shrinks. The volumes are trajectories reached by the end-effector lifting different loads, with joints programmed to oscillate at various frequencies.

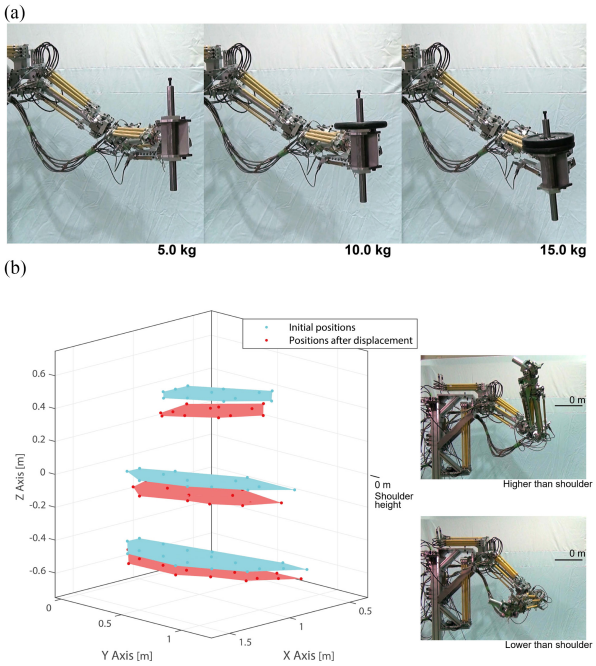

Fig. 7. Volume-constant compliance of the power soft robot under different loads: (a) Passive displacement caused by addings 5 kg loads with the valve closed. (b) Passive displacement caused by a 10 kg load: The blue points correspond to the initial end-effector positions, and the red points indicate the positions after displacement. Cross sections from the 0 kg condition in Fig. 6(c) were arbitrarily selected for three different heights: above, at, and below the shoulder (0 m on the Z-axis). Experiments were conducted multiple times for each height.

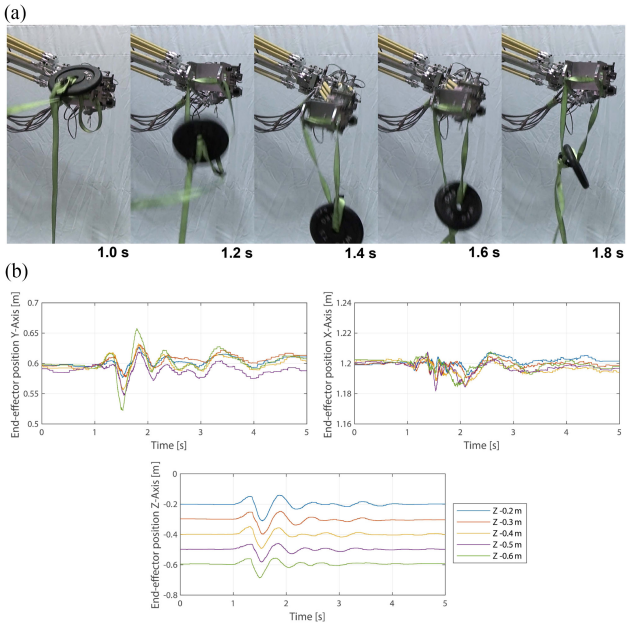

Fig. 8. Impact reactions of the 7-DOF power soft robot: (a) Reactions immediately after being impacted by a 5 kg load falling from a height of 0.5 m at 1.0 s. (b) Reactions at different heights: Z-axis data represents position changes in the vertical direction, while Y-axis and X-axis data indicate the degree of lateral and forward oscillation, respectively.

2) End-Effector Compliance: We introduce two types of compliance: volume-constant compliance and pressure-constant compliance. The volume-constant compliance assumes that all valves are fully closed while pressure changes. Pressure-constant compliance maintains constant pressure throughout all muscles.

The proposed Algorithm 2 is designed to determine compliance for reachable poses, as illustrated by an example under a 100 N force in Fig. 4. Pressure-constant compliance demonstrates higher compliance within the range of 5 to 20 mm/N as the torque change is solely due to the change in muscle contraction ratio (refer Fig. 5(c)). Conversely, volume-constant compliance is stiffer, caused by combining changes in pressure and changes in contraction ratio. Nevertheless, for the majority of reachable poses, the volume-constant compliance ranges from 0.5 to 2.0 mm/N (refer Fig. 5(d)).

III. Experimental Results

Here, we introduce the experimental workable and payload capacity of the robot (Fig. 6), followed by an analysis of compliance (Fig. 7). Subsequently, we evaluate its impact resistance ability (Fig. 8). Finally, we conduct a concrete chipping experiment (Fig. 9).

A. Workspace and Payload

As depicted in Fig. 6(b), the proposed power soft robot successfully lifted a 25 kg load (four 5 kg barbell plates and 5 kg of barbell bar and its fixations). To evaluate the relationship between the payload and the robot's reachable workspace, we conducted experiments with different loads attached to the robot's end. In each experiment, joints were programmed to oscillate within achievable angular positions at various frequencies for over 10 minutes, and the trajectories reached by the end-effector were recorded. The volumes covered by these trajectories were then plotted, as illustrated in Fig. 6(c).

The experimental workspace with a 0-kg payload has a similar shape but is smaller than the predicted 0-kg payload workspace results in Fig. 5. One of the primary reasons for this limitation is the residual pressure in the muscles, approximately 0.5 MPa, which leads to the elongated muscles generating significant forces, thereby restricting the range of motion of the joints. Consistent with predictions in Figs. 5(b), and 6(c) illustrates that the payload capacity is correlated with the robot's pose, showing a greater lifting capacity in the lower position. The robot could lift a 5 kg load to a higher position well above the shoulder height (>0 m on the Z axis), or lift a 25 kg load to a position 0.5 m lower than shoulder height. Thus, the 7-DOF power soft robot demonstrates a high lifting capacity of over 25 kg, despite the restricted workspace.

B. Volume-Constant Compliance

An example of volume-constant compliance under loads is shown in Fig. 7(a), which adds 5 kg barbell plates to the barbell bar fixed to the end. To confirm that compliance is also significantly related to position height, similar to payload capacity, we selected three cross-sections at different heights within the robot's workspace under the 0 kg load condition (refer Fig. 6(c)). Using position-only control, we moved the end-effector to multiple positions on the three cross-sections. Subsequently, we set the servovalve to a nearly neutral position

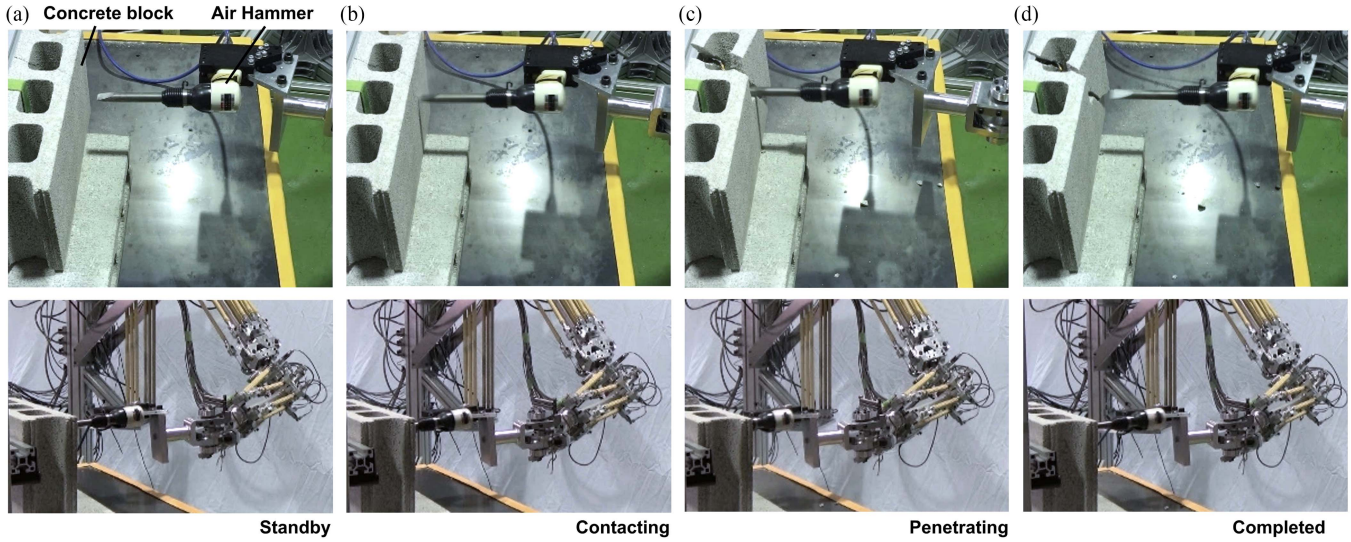

Fig. 9. Concrete block chipping experiment of 7-DOF power soft robot using an air hammer: (a) Air hammer initiated in standby state. (b) The robot moves the air hammer into contact with the concrete block. (c) The robot applies forward force to penetrate the concrete block. (d) Completion of the operation, returning to the initial position. The 7-DOF power soft robot stably conducts all the steps under a pressure of 5.0 MPa, indicating high vibration resistance and stability.

to block the oil outlets of the muscles, ensuring minimal oil leakage. Following this, a 10 kg load was attached to the end, resulting in a downward displacement. Results are illustrated in Fig. 7(b).

At a height of 0.5 m above the shoulder with 12 samplings, the mean vertical volume-constant compliance is 1.19 mm/N. at the same height as the shoulder and 0.5 m lower with 13 and 18 samplings, the mean compliance is 1.07 mm/N and 0.60 mm/N, respectively. It is consistent with the prediction results in Fig. 5(d) within 0.5–2.0 mm/N. This trend that higher positions have more compliance is not obvious in the simulation. This is primarily attributed to inaccuracies in the approximate models utilized in the simulation. Unlike PAMs, which use compressible fluid, the pressure changes in HAMs are much more sensitive to small changes in contraction, making them more challenging to model accurately.

The experimental results validate that the power soft robot exhibits inherent compliance while maintaining a larger payload capacity. It achieves volume-constant compliance at the 0.5–2.0 mm/N level without additional compliant mechanisms, which can add weight and complexity, or active compliance control systems requiring additional sensors.

C. Impact Experiment

We conducted experiments involving a 5 kg load attached to the end of the robotic arm using a 0.5 m strap to assess the impact resistance of the artificial muscles. The servovalves were closed, and the load was dropped to simulate an impact on the end of the arm. The experiment was repeated at various Z-axis positions with constant positions of the other axes and orientations. The resulting change in the position of the robot end-effector is depicted in Fig. 8(b). A continuous image in Fig. 8(a), shows the results for the −0.2 m height for the 1.0 to 2.0 s of the instant of weight fall at intervals of 0.2 s.

These results demonstrate how the position of the end-effector on the Z-axis varies in response to the impact. When the load is dropped at 1.0 s, the arm initially experiences a slight upward displacement due to its compliance. At 1.4 s, the arm undergoes an impact caused by the 0.5 m falling load, significantly changing its Z-axis position more than 0.1 m. The subsequent 2 seconds experienced fewer than five noticeable oscillations and returned to a stable state. Due to the robot's pose being lifted to the left, there were noticeable oscillations in the Y-axis and minor oscillations in the X-axis after the impact. Unlike the PAM robot, the hydraulic actuation in the HAM robot prevents violent reactions in response to strong disturbances.

The robot can easily withstand impacts without any damage owing to the absorption of impact by HAMs. This feature, combined with its lightweight and structurally concise design, positions it as better suited for tasks involving repetitive impacts compared to many other multi-DOF robots. This is particularly relevant in applications like hammering in construction or manufacturing, where the robot must maintain stability and reliability despite enduring frequent impacts.

D. Concrete Chipping Experiment

We conducted a concrete chipping experiment to validate the vibration resistance of the robot. For this experiment, we used an air hammer to chip away at a concrete block. The chipping procedure is demonstrated in Fig. 9. The power soft robot is controlled to gently make contact with the surface of the concrete block using the air hammer, and then to penetrate it with a strong forward force.

This experiment assessed the robot's ability to withstand vibrations and maintain stability and functionality. The air hammers generate intense vibrations, and HAMs absorb the vibrations. Moreover, the "Softness" of soft contact with the surface of the concrete block and strong pushing "Powerfulness" was demonstrated. Unlike other heavy hydraulic machines, this compliant power soft robot can be potentially used for tasks involving high-vibration environments alongside a human operator, offering flexibility and adaptability in various industrial applications.

IV. Conclusion

This study introduced a 7-DOF power soft robot driven by hydraulic McKibben artificial muscles (HAMs). The robot demonstrates inherent compliance, high payload capacity, and strong impact and vibration resistance, allowing safe human-robot interactions and versatile performance in various environments.

Despite having a more restricted workspace than conventional robots, it can lift weights up to 25 kg. The lower the end-effector, the higher the robot's payload capacity. The robot achieves volume-constant compliance ranging from 0.5 to 2.0 mm/N volume-constant compliance without active control, as demonstrated through the simulations and experiments. Additionally, simulation results demonstrate pressure-constant compliance ranging from 5 to 20 mm/N. Experimental evaluations have also demonstrated a high impact capacity, as evidenced by its ability to withstand a 5 kg load falling from a height of 0.5 m, and a vibration-resistance capacity when subjected to an air hammer's recoil. Hence, the practicality of the hydraulic muscle-driven power soft robot was experimentally validated.

In future research, our aim is to develop control methods to optimize the performance of the power soft robot by leveraging the characteristics of its antagonistic joints and redundancy of 7-DOF. Then, we will explore various field applications that can effectively utilize its impact and vibration-resistance capacities, in addition to its passive compliance.

References

[1] "Bionic cobot." Accessed: Oct. 17, 2023. [Online]. Available: https://www.festo.com/us/en/e/about-festo/research-and-development/bionic-learning-network/highlights-from-2015-to-2017/bioniccobot-id_33294

[2] "Bionic motion robot." Accessed: Oct. 17, 2023. [Online]. Available: https://www.festo.com/us/en/e/about-festo/research-and-development/bionic-learning-network/highlights-from-2015-to-2017/bionicmotionrobot-id_33307

[3] "Bionic soft arm." Accessed: Oct. 17, 2023. [Online]. Available: https://www.festo.com/us/en/e/about-festo/research-and-development/bionic-learning-network/highlights-from-2015-to-2017/bionicsoftarm-id_68209

[4] M. Hofer, J. Zughaibi, and R. D'Andrea, "Design and control of an inflatable spherical robotic arm for pick and place applications," *Actuators*, vol. 10, 2021, Art. no. 299.

[5] H.-J. Kim, A. Kawamura, Y. Nishioka, and S. Kawamura, "Mechanical design and control of inflatable robotic arms for high positioning accuracy," *Adv. Robot.*, vol. 32, no. 2, pp. 89–104, 2018.

[6] M. Takeichi, K. Suzumori, G. Endo, and H. Nabae, "Development of a 20-m-long Giacometti arm with balloon body based on kinematic model with air resistance," in *Proc. IEEE/RSJ Int. Conf. Intell. Robots Syst.*, 2017, pp. 2710–2716.

[7] B. Mazzolai et al., "Roadmap on soft robotics: Multifunctionality, adaptability and growth without borders," *Multifunctional Mater.*, vol. 5, no. 3, 2022, Art. no. 032001.

[8] Airic's arm. Accessed: Jun. 27, 2022. [Online]. Available: https://www.festo.com/gb/en/e/about-festo/research-and-development/bionic-learning-network/highlights-from-2006-to-2009/airic-s-arm-id_33870/

[9] B. Tondu, S. Ippolito, J. Guiochet, and A. Daidie, "A seven-degrees-of-freedom robot-arm driven by pneumatic artificial muscles for humanoid robots," *Int. J. Robot. Res.*, vol. 24, no. 4, pp. 257–274, 2005.

[10] P. Ohta et al., "Design of a lightweight soft robotic arm using pneumatic artificial muscles and inflatable sleeves," *Soft Robot.*, vol. 5, no. 2, pp. 204–215, 2018.

[11] Y. Okazaki, M. Komatsu, Y. Tsusaka, and M. Yamamoto, "Development of a human safe, multi-degree-of-freedom robot arm technology using pneumatic muscles," *J. Robot. Soc. Jpn.*, vol. 28, no. 3, pp. 302–310, 2010.

[12] B. M. Pritts and C. D. Rahn, "Design of an artificial muscle continuum robot," in *Proc. IEEE Int. Conf. Robot. Automat.*, 2004, pp. 4742–4746.

[13] A. Niikura et al., "Giraffe neck robot: First step toward a powerful and flexible robot prototyping based on giraffe anatomy," *IEEE Robot. Automat. Lett.*, vol. 7, no. 2, pp. 3539–3546, Apr. 2022.

[14] A. Nikkhah, C. Bradley, and A. S. Ahmadian, "Design, dynamic modeling, control and implementation of hydraulic artificial muscles in an antagonistic pair configuration," *Mechanism Mach. Theory*, vol. 153, 2020, Art. no. 104007.

[15] M. Meller, J. Chipka, A. Volkov, M. Bryant, and E. Garcia, "Improving actuation efficiency through variable recruitment hydraulic McKibben muscles: Modeling, orderly recruitment control, and experiments," *Bioinspiration Biomimetics*, vol. 11, no. 6, 2016, Art. no. 065004.

[16] M. Mori, K. Suzumori, S. Seita, M. Takahashi, T. Hosoya, and K. Kusumoto, "Development of very high force hydraulic McKibben artificial muscle and its application to shape-adaptable power hand," in *Proc. IEEE Int. Conf. Robot. Biomimetics*, 2009, pp. 1457–1462.

[17] S. Kittisares, H. Nabae, G. Endo, K. Suzumori, and R. Sakurai, "Design of knee support device based on four-bar linkage and hydraulic artificial muscle," *Robomech J.*, vol. 7, no. 1, pp. 1–10, 2020.

[18] Z. Mao, Y. Asai, A. Yamanoi, Y. Seki, A. Wiranata, and A. Minaminosono, "Fluidic rolling robot using voltage-driven oscillating liquid," *Smart Mater. Structures*, vol. 31, no. 10, 2022, Art. no. 105006.

[19] Y. Feng et al., "Experimental comparison of antagonistic hydraulic muscle actuation under single/dual and zero/overlapped servovalve configurations," *Mechatronics*, vol. 83, 2022, Art. no. 102737.